

Research Article

Open Access



# A novel structure Ti/Fe<sub>2</sub>O<sub>3</sub>/Cu<sub>2</sub>S/Co(OH)<sub>x</sub> enhances the photoelectrochemical water splitting performance of iron oxide

Hao-Yan Shi<sup>1,2,3</sup>, Yan-Xin Chen<sup>1,2,3,4,\*</sup> , Ming-Hao Ji<sup>1,3</sup>, Qian-Qian Zhou<sup>1,3</sup>, Ke-Xian Li<sup>1,3</sup>, Hai-Long Wang<sup>1,3</sup>, Rui Chen<sup>1,3</sup>, Xiu-Mei Lin<sup>5,\*</sup> , Can-Zhong Lu<sup>1,2,3,4,\*</sup>

<sup>1</sup>State Key Laboratory of Structural Chemistry, Fujian Institute of Research on the Structure of Matter, Chinese Academy of Sciences, Fuzhou 350002, Fujian, China.

<sup>2</sup>School of Chemical Sciences, University of Chinese Academy of Sciences, Beijing 100049, China.

<sup>3</sup>Xiamen Key Laboratory of Rare Earth Photoelectric Functional Materials, Xiamen Institute of Rare-earth Materials, Haixi Institutes, Chinese Academy of Sciences, Xiamen 361021, Fujian, China.

<sup>4</sup>Fujian Science & Technology Innovation Laboratory for Optoelectronic Information of China, Fuzhou 350108, Fujian, China.

<sup>5</sup>College of Chemistry, Chemical Engineering and Environment, Fujian Province University Key Laboratory of Analytical Science, Minnan Normal University, Zhangzhou 363000, Fujian, China.

\*Correspondence to: Prof. Yan-Xin Chen, Prof. Can-Zhong Lu, State Key Laboratory of Structural Chemistry, Fujian Institute of Research on the Structure of Matter, Chinese Academy of Sciences, 155 Yangqiao Road West, Fuzhou 350002, Fujian, China. E-mail: yanxinchen@fjirsm.ac.cn; czlu@fjirsm.ac.cn; Dr. Xiu-Mei Lin, College of Chemistry, Chemical Engineering and Environment, Fujian Province University Key Laboratory of Analytical Science, Minnan Normal University, 36 Xianqian Street, Zhangzhou 363000, Fujian, China. E-mail: xiu-mei.lin@xmu.edu.cn

**How to cite this article:** Shi HY, Chen YX, Ji MH, Zhou QQ, Li KX, Wang HL, Chen R, Lin XM, Lu CZ. A novel structure Ti/Fe<sub>2</sub>O<sub>3</sub>/Cu<sub>2</sub>S/Co(OH)<sub>x</sub> enhances the photoelectrochemical water splitting performance of iron oxide. *Chem Synth* 2024;4:45. <https://dx.doi.org/10.20517/cs.2023.68>

**Received:** 22 Dec 2023 **First Decision:** 16 Apr 2024 **Revised:** 25 Jun 2024 **Accepted:** 5 Jul 2024 **Published:** 7 Aug 2024

**Academic Editor:** Aicheng Chen **Copy Editor:** Pei-Yun Wang **Production Editor:** Pei-Yun Wang

## Abstract

The slow oxygen evolution kinetics of iron oxide nanorod arrays have limited their applications in photocatalytic water splitting. Herein, we introduce p-type semiconductor cuprous oxide and further cover cobalt hydroxide ultrathin nanosheets on the surface of both by electrochemical deposition; these methods obviously enhanced the photoelectrochemical (PEC) water splitting performance of iron oxide nanorods on titanium sheet substrate. The photocurrent of this heterostructure reached 4.8 mA/cm<sup>2</sup> at 1.23 V (vs. reversible hydrogen electrode) in a 1 M KOH aqueous solution under AM 1.5G illumination, which is much higher than the currently reported photocatalytic water splitting performance of iron oxide nanoarrays. The construction of Fe<sub>2</sub>O<sub>3</sub>/Cu<sub>2</sub>S p-n heterojunction accelerates the separation of photogenerated carriers in the main body of Fe<sub>2</sub>O<sub>3</sub> nanorod arrays; as an excellent oxygen evolution catalyst (OEC), the introduction of Co(OH)<sub>x</sub> accelerates the kinetic process of



© The Author(s) 2024. **Open Access** This article is licensed under a Creative Commons Attribution 4.0 International License (<https://creativecommons.org/licenses/by/4.0/>), which permits unrestricted use, sharing, adaptation, distribution and reproduction in any medium or format, for any purpose, even commercially, as long as you give appropriate credit to the original author(s) and the source, provide a link to the Creative Commons license, and indicate if changes were made.



interfacial water oxidation leading to the rapid depletion of photogenerated holes, which further improves the charge separation on the photoanode surface. Thus, the synergistic effect between  $\text{Fe}_2\text{O}_3/\text{Cu}_2\text{S}$  p-n heterojunctions and oxygen evolution catalysts enhanced the iron oxide nanorod array photoanodes.

**Keywords:**  $\text{Ti}/\text{Fe}_2\text{O}_3/\text{Cu}_2\text{S}/\text{Co}(\text{OH})_x$ , photoelectrochemical, water splitting, hydrogen evolution

## INTRODUCTION

With economic and social development, the energy and environmental crises are increasingly becoming a constraint on human progress<sup>[1]</sup>, but the photoelectrochemical (PEC) water splitting into hydrogen<sup>[2]</sup> offers a promising solution that exploits nature's most abundant solar energy to decompose the earth's vastly more abundant water resources into clean, environmentally friendly, and highly energy-dense hydrogen<sup>[3]</sup>. In 1972, Fujishima and Honda demonstrated the potential of titanium dioxide ( $\text{TiO}_2$ )<sup>[4]</sup> semiconductor materials in splitting water into hydrogen and oxygen in photochemical cells<sup>[5]</sup>.

Many highly active photoanodes have been reported, such as a monoclinic tungsten trioxide ( $\text{WO}_3$ ) nanowire by Nayak *et al.*<sup>[6]</sup>. The PEC activity of this nanowire was about 21 times higher than that of  $\text{WO}_3$ - $\text{H}_2\text{O}$  nanoplates and higher than that of the existing  $\text{WO}_3$  nanostructures. The enhanced PEC activity is attributed to the one-dimensional morphology of the  $\text{WO}_3$  nanowires, larger surface area, and other factors.

Among the numerous semiconductor photoelectric anode materials, hematite<sup>[7]</sup> ( $\alpha\text{-Fe}_2\text{O}_3$ ) has become one of the most widely applied photoanode materials at this stage because of its excellent stability and environmental friendliness<sup>[8,9]</sup>.  $\text{Fe}_2\text{O}_3$  has a band gap ( $E_g$ ) of 1.9 to 2.2 eV<sup>[10]</sup>. Therefore, its light absorption range exceeds 600 nm, and it has sufficient visible light absorption<sup>[11]</sup>; theoretical calculations show that an ideal  $\text{Fe}_2\text{O}_3$  photoanode can achieve up to 12.6  $\text{mA}/\text{cm}^2$  at 1.23 V [vs. reversible hydrogen electrode (RHE)] under 100  $\text{mW}/\text{cm}^2$  (AM 1.5G) of solar radiation<sup>[12]</sup>. However, the actual performance of  $\text{Fe}_2\text{O}_3$  in PEC cells falls significantly below the theoretical value due to fast carrier complexation and a short hole diffusion length (only 2-4 nm), which severely affects its practical application<sup>[8]</sup>. Various modification strategies have been used to alleviate the shortcomings of hematite, such as doping<sup>[13]</sup>, homojunction<sup>[14]</sup>/heterojunction<sup>[15]</sup> formation, and surface modification<sup>[16]</sup>.

$\text{Cu}_2\text{S}$  is a widely utilized p-type semiconductor commonly employed in solar energy conversion<sup>[17]</sup>. It has an excellent ability to absorb light utilizing a wide range of wavelengths<sup>[18]</sup>, while its high conductivity permits efficient photogenerated charge transfer<sup>[19]</sup>. A recent report has shown that the heterostructure formed by  $\text{Fe}_2\text{O}_3$  and  $\text{Cu}_2\text{S}$  exhibits enhanced photocatalytic activity under oxygen evolution reaction (OER). The enhanced activity is attributed to the formation of covalent bonds between  $\text{Cu}_2\text{S}$  and  $\text{Fe}_2\text{O}_3$ , particularly the S-O bonds<sup>[20]</sup>.

The construction of p-n junctions has been shown to optimize the PEC performance of photoanode arrays<sup>[21]</sup>. The built-in electric field facilitates the rapid separation of photogenerated carriers at the p-n junction<sup>[22]</sup> interface. It reduces bulk phase complexation, thereby enhancing the PEC water-splitting performance of the photoanode<sup>[23]</sup>. For instance, using the Ar plasma-assisted strategy, Meng *et al.* fabricated a  $\text{SnS}_2$  nanosheet array with numerous surface holes<sup>[24]</sup>. The reduction property of Ar atoms led to a partial reduction of  $\text{Sn}^{4+}$  to  $\text{Sn}^{2+}$ , forming a  $\text{SnS}/\text{SnS}_2$  p-n junction of the nanosheet array. This facilitates carrier separation and prolongs carrier lifetime. As a result, the photocurrent density of this nanosheet array was 2.15  $\text{mA}/\text{cm}^2$ . In addition, Wu *et al.* also synthesized atomic sandwiched nitrogen-doped  $\text{SnS}_2$

nanosheets (p-n-p-SnS<sub>2</sub>) by controlled NH<sub>3</sub> treatment<sup>[25]</sup>. The best sample achieved an optical current density of 3.28 mA/cm<sup>2</sup>. The outstanding performance can be attributed to the formation of p-n-p junctions that facilitate electron-hole transfer and optimize the kinetics of the oxygen precipitation reaction. Notably, loaded oxygen precipitation catalysts [oxygen evolution catalysts (OECs)] are considered a particularly effective method for enhancing the surface reaction kinetics of  $\alpha$ -Fe<sub>2</sub>O<sub>3</sub> membranes<sup>[26]</sup>. The OECs used in PEC systems are usually derived from superior electrocatalysts, and many of these low-cost transition-metal-based OECs have been shown to be able to achieve low overpotentials for electrochemical OER<sup>[27]</sup>.

The construction of ternary photocatalytic or PEC materials has been widely studied. For example, Yang *et al.* reported a photocatalyst TiO<sub>2</sub>/MgTiO<sub>3</sub>/C that was synthesized at the gram scale by a simple mechanochemical method<sup>[28]</sup>. The ternary heterostructure achieves excellent light utilization and good photostability and is more conducive to solar-driven photochemical hydrogen production. An *et al.* achieved the co-synthesis of H<sub>2</sub>O<sub>2</sub> and hydrogen by constructing a ternary photoanode CaSnO<sub>3</sub>/SrTiO<sub>3</sub>/BiVO<sub>4</sub> (CSO/STO/BVO), replacing the four-electron reaction with the kinetically superior two-electron reaction optimized the kinetics of the water oxidation of the PEC and facilitated the separation of the products<sup>[29]</sup>. In addition, the authors performed outdoor tests and considered issues for practical engineering applications.

However, simultaneous improvement in charge separation and surface oxygen precipitation kinetics at  $\alpha$ -Fe<sub>2</sub>O<sub>3</sub> nanorod array photoanodes through synergistic effects between p-n heterojunctions and OECs has not yet been achieved.

Herein, we grew an array of Fe<sub>2</sub>O<sub>3</sub> nanorods on titanium sheets using a hydrothermal method, which was used as a photoanode named Ti/Fe<sub>2</sub>O<sub>3</sub>. Further, we introduced a p-type semiconductor cuprous sulfide to form a p-n heterojunction photoanode (named Ti/Fe<sub>2</sub>O<sub>3</sub>/Cu<sub>2</sub>S), which significantly enhanced the PEC water-oxidation performance of the photoanode. In addition, the surfaces of both were further covered with ultrathin nanosheets of cobalt hydroxide by electrochemical deposition, which also significantly improved the PEC water decomposition performance of the Ti/Fe<sub>2</sub>O<sub>3</sub>/Cu<sub>2</sub>S photoanode. The photocurrent of this heterostructure [named Ti/Fe<sub>2</sub>O<sub>3</sub>/Cu<sub>2</sub>S/Co(OH)<sub>x</sub>] reached 4.8 mA/cm<sup>2</sup> at 1.23 V (vs. RHE) in 1 M KOH aqueous solution at AM 1.5G, which is much higher than the PEC water splitting performance of the Fe<sub>2</sub>O<sub>3</sub> nanoarrays reported so far. The substantial improvement of the catalytic performance is mainly attributed to two points: one is that the introduction of Fe<sub>2</sub>O<sub>3</sub>/Cu<sub>2</sub>S p-n heterojunction accelerates the separation of photogenerated carriers in the Fe<sub>2</sub>O<sub>3</sub> nanorod arrays; the other is that the addition of OEC on the Co(OH)<sub>x</sub> surface accelerates the kinetics of the interfacial water oxidation, and the rapid depletion of the photogenerated holes further improves the photo-anodic surface charge separation. Therefore, the synergistic effect between Fe<sub>2</sub>O<sub>3</sub>/Cu<sub>2</sub>S p-n heterojunction and OEC significantly enhances the PEC water decomposition performance of the iron oxide nanorod array photoanode.

## EXPERIMENTAL

### Materials and synthesis methods

All chemical reagents used were analytically pure and underwent no further refinement during the experiment, including titanium foil, concentrated hydrochloric acid, acetone (C<sub>3</sub>H<sub>6</sub>O), ethanol absolute (C<sub>2</sub>H<sub>6</sub>O), deionized water, FeCl<sub>3</sub>·6H<sub>2</sub>O, NaNO<sub>3</sub>, Co(NO<sub>3</sub>)<sub>2</sub>·6H<sub>2</sub>O, CuCl, and Na<sub>2</sub>S·9H<sub>2</sub>O.

#### Preparation of Ti/Fe<sub>2</sub>O<sub>3</sub> photoanode

The Ti/Fe<sub>2</sub>O<sub>3</sub> nanorod photoelectrode was prepared by a simple hydrothermal method<sup>[7]</sup> [Figure 1]. Firstly, 182.4 mg of FeCl<sub>3</sub>·6H<sub>2</sub>O and 383 mg of NaNO<sub>3</sub> were dissolved in 4.5 mL of ultrapure water, and the

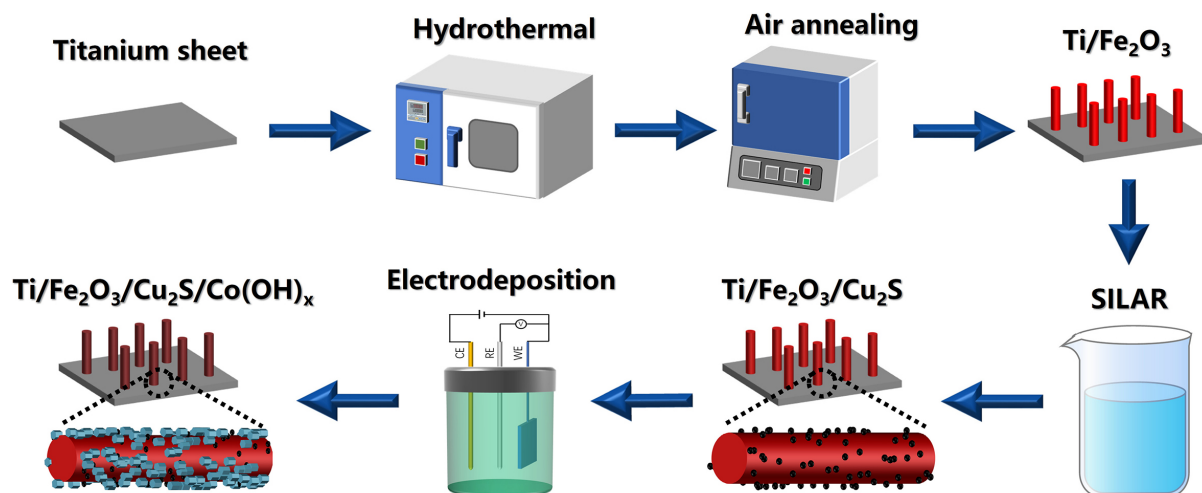


**Figure 1.** Synthesis steps of Ti/Fe<sub>2</sub>O<sub>3</sub>/Cu<sub>2</sub>S/Co(OH)<sub>x</sub> photoanode.

resulting solution was stirred continuously for 2 h before adding 20  $\mu$ L concentrated hydrochloric acid. Next, the prepared mixed solution of 0.15 M FeCl<sub>3</sub> and 1 M NaNO<sub>3</sub> was transferred to the stainless steel autoclave lined with polytetrafluoroethylene, and the titanium sheet was also immersed in the solution. After that, the autoclave was put into the oven and heated at 100  $^{\circ}$ C (1  $^{\circ}$ C/min) for 5 h. After the reaction, the titanium sheet was deposited with a uniform yellow  $\beta$ -FeOOH layer. Finally, the substrate was washed with deionized water to remove residual FeOOH and calcined at 550  $^{\circ}$ C (2  $^{\circ}$ C/min) for 2 h to obtain a sample called Ti/Fe<sub>2</sub>O<sub>3</sub>. The titanium sheets used in the hydrothermal reaction were ultrasonically cleaned in advance with a mixture of hydrochloric acid, ethanol acetone, and deionized water for 0.5 h to remove organic pollutants and dust.

#### Preparation of Ti/Fe<sub>2</sub>O<sub>3</sub>/Cu<sub>2</sub>S photoanode

According to previous reports, Ti/Fe<sub>2</sub>O<sub>3</sub>/Cu<sub>2</sub>S heterostructures were synthesized using the successive ion layer adsorption and reaction (SILAR) method<sup>[18]</sup> [Figure 1]. The  $\alpha$ -Fe<sub>2</sub>O<sub>3</sub> nanorod photoelectrode was first immersed in a CuCl-saturated solution for 60 s, which allowed Cu<sup>+</sup> to adsorb on the surface of the  $\alpha$ -Fe<sub>2</sub>O<sub>3</sub> nanorod photoelectrode. Then, the photoelectrode was rinsed in deionized water for 60 s to prevent excessive Cu<sub>2</sub>S precipitation. Afterward, the photoelectrode was immersed in 5 mM Na<sub>2</sub>S anion solution for 60 s to react S<sup>2-</sup> with adsorbed Cu<sup>+</sup> to produce Cu<sub>2</sub>S. Finally, the photoelectrode was rinsed with deionized water for 60 s. These steps constitute a cycle count. The photoelectrode was immersed in the solution for different cycles (3, 5, 10, 15) to control the deposition amount of Cu<sub>2</sub>S. Finally, the photoelectrode synthesized by the SILAR method was annealed in an argon atmosphere at 200  $^{\circ}$ C (5  $^{\circ}$ C/min) for 2 h, resulting in a sample called Ti/Fe<sub>2</sub>O<sub>3</sub>/Cu<sub>2</sub>S.

#### Preparation of Ti/Fe<sub>2</sub>O<sub>3</sub>/Cu<sub>2</sub>S/Co(OH)<sub>x</sub> photoanode

According to previous reports<sup>[27]</sup>, the photoelectrode Ti/Fe<sub>2</sub>O<sub>3</sub>/Cu<sub>2</sub>S/Co(OH)<sub>x</sub> was synthesized through a simple electrochemical deposition method [Figure 1]. Using a 1 mA/cm<sup>2</sup> cathode current density, Ti/Fe<sub>2</sub>O<sub>3</sub>/Cu<sub>2</sub>S photoelectrode was deposited onto ultra-thin Co(OH)<sub>x</sub> nanosheets in a solution containing 2 mM Co(NO<sub>3</sub>)<sub>2</sub>. The best performance of the photoelectrode could be achieved by selecting different deposition times (30, 60, 90, and 120 s). The final sample obtained was called Ti/Fe<sub>2</sub>O<sub>3</sub>/Cu<sub>2</sub>S/Co(OH)<sub>x</sub>.

### Preparation of Cu<sub>2</sub>S nanoparticles

The saturated CuCl and 5 mM Na<sub>2</sub>S solutions were mixed with thorough stirring, and the Cu<sub>2</sub>S nanoparticles were obtained after pumping and filtering. After acid washing and centrifugation, the obtained Cu<sub>2</sub>S nanoparticles were deposited on fluorine-doped tin oxide (FTO) by spin coating for electrochemical testing.

### Materials characterizations

The microscopic morphology was evaluated using a scanning electron microscope (SEM, Apreo S LoVac, Thermo Fisher Scientific) with an operating voltage of 10 kV. The TF20 (FEI), operated at 200 kV, was used to perform transmission electron microscopy (TEM) and selected area electron diffraction (SAED) techniques to characterize the detailed morphology, size, and element composition of the samples. The crystal structure of the sample was described using X-ray diffraction (XRD) data obtained from the Miniflex 600 X-ray diffractometer. The measurement range was 20°-80° with CuK radiation. The light absorption ability of the sample was evaluated by collecting the ultraviolet-visible (UV-vis) absorption spectrum using the Cary 5000 spectrophotometer (Agilent). X-ray photoelectron spectroscopy (XPS) was performed with Al Ka rays.

The bandgap energy ( $E_g$ ) is determined from UV-vis diffuse reflectance spectroscopy (UV-vis-DRS), specifically utilizing the Tauc diagram.  $E_g$  is calculated using:

$$(ah\nu)^x = A(h\nu - E_g) \quad (1)$$

Which represents Tauc plotting, where  $a$  is the direct light absorption coefficient,  $h$  is Planck's constant,  $\nu$  is the frequency of the incident light,  $A$  is the proportionality constant, and  $E_g$  is the energy gap of the semiconductor photocatalyst. For direct bandgap semiconductors,  $x$  equals 2; for indirect bandgap semiconductors,  $x$  equals 1/2.

### PEC measurements

The PEC test was conducted using a PEC2000 PEC test system (Beijing Perfectlight Technology Co., Ltd., Beijing, China), which comprises a Shanghai Chenhua electrochemical workstation (CHI760e), a xenon lamp (PLS-FX300HU, Beijing Perfectlight) with an AM 1.5G filter (100 mW/cm<sup>2</sup>), a chopper module (PFS40A shutter actuator), and a single-room electrochemical cell. The PEC tests were conducted under no light, light, or alternating light conditions. Linear sweep voltammetry (LSV) typically measured the potential range between -0.31 and 0.61 V (vs. Ag/AgCl), with light intermittently blocked by a shutter toggling every 5 s. Chronoamperometric testing (I-t) was performed at 0.23 V (vs. Ag/AgCl) under light conditions. The prepared photoelectric electrode served as the working electrode, a Pt plate as the counter electrode, Ag/AgCl (saturated KCl) as the reference electrode, and 1 M KOH (pH = 13.6) as the electrolyte. Throughout the testing, it was ensured that the working electrode had a light-exposed area of 1 cm<sup>2</sup>. The measured potential could be converted to  $E_{RHE}$  (V) value using:

$$E_{RHE} = E_{Ag/AgCl} + 0.0592 \times \text{pH} + E_{Ag/AgCl}^0 \quad (2)$$

Where  $E_{Ag/AgCl}^0 = 0.1976$  V vs. RHE (25 °C).

The applied bias photon-to-current efficiency (ABPE) with external bias can be calculated using:

$$ABPE(\%) = \frac{J_{ph} \times (1.23 \text{ V} - E_{app})}{P_{light}} \times 100\% \quad (3)$$

Where  $J_{ph}$  denotes the photocurrent density ( $\text{mA}/\text{cm}^2$ ) measured by the electrochemical workstation.  $E_{app}$  signifies the relationship between the applied bias voltage and  $E_{RHE}$  (V), and  $P_{light}$  represents the total light intensity of AM 1.5G ( $100 \text{ mW}/\text{cm}^2$ ).

The incident monochromatic photon electron conversion efficiency (IPCE) and Mott-Schottky (MS) measurements were conducted in the IPCE1000 PEC testing system (Beijing Perfectlight Technology Co., Ltd., Beijing, China). The instrument is equipped with an electrochemical workstation (CS 350H, Wuhan Kotex Instruments Co., Ltd., China). IPCE can be calculated by:

$$IPCE(\%) = 1240 \times [I_{ph}/(\lambda \times P_{in})] \times 100\% \quad (4)$$

Where  $I_{ph}$  ( $\text{A}/\text{cm}^2$ ) refers to the output photocurrent density at each wavelength ( $\lambda$ , nm), and  $P_{in}$  represents the incident light power density. Usually, the IPCE spectrum is calculated based on the photocurrent density recorded by the chronoamperometric method. The incident monochromatic light of 300-600 nm is separated by a monochromator using a xenon lamp (PLS-FX300HU, Beijing Perfectlight).

The MS measurement results were used to illustrate the flat band potentials. The frequency range of the electrochemical analyzer is 0.1~100,000 Hz. The working electrodes were measured at 500, 1,000, 1,500, and 2,000 Hz, respectively. Based on the MS plot, the flat band potential of the photoelectrode can be determined according to:

$$\frac{1}{C^2} = \frac{2}{e\epsilon_0\epsilon N_D} \left[ (E - E_{FB}) - \frac{\kappa T}{e} \right] \quad (5)$$

Where  $C$  is the space charge capacitance,  $e$  is the electron charge,  $\epsilon$  is the vacuum permittivity ( $8.85 \times 10^{-12} \text{ F}\cdot\text{m}^{-1}$ ),  $\epsilon_0$  is the relative permittivity of hematite ( $\epsilon_0 = 80$ ),  $N_D$  is the charge donor density, which, in this case, can refer to the carrier concentration ( $\text{cm}^{-3}$ ),  $E$  is the electrode applied potential,  $E_{FB}$  is the flat charged potential,  $\kappa$  is the Boltzmann constant ( $1.38 \times 10^{-23} \text{ J}\cdot\text{K}^{-1}$ ), and  $T$  is the absolute temperature (K).

The carrier concentration ( $N_D$ ) of the obtained photoanode can be roughly estimated by:

$$N_D = \frac{2}{e\epsilon_0\epsilon} \left[ \frac{d\left(\frac{1}{C^2}\right)}{dE} \right]^{-1} \quad (6)$$

Electrochemical impedance spectroscopy (EIS) was performed using a Squidstat Plus electrochemical workstation (Admiral Instruments, Tempe, Arizona, USA).

PEC  $\text{H}_2$  evolution experiments were conducted using an all-glass automatic online trace gas analysis system (Labsolar-6A, Beijing Perfectlight). The system utilized a xenon lamp (Microsolar 300, Beijing Perfectlight). This setup was interfaced with a commercial electrochemical workstation (Squidstat Plus, Admiral Instruments, Arizona) for bias voltage application (0.23 V vs. Ag/AgCl) and photocurrent data collection. The electrolyte used was a 1 M KOH solution (75 mL). Periodic analysis of PEC-generated  $\text{H}_2$  was performed using a FULI-GC-9790II gas chromatograph (GC) (Zhejiang Fuli) equipped with a thermal conductivity detector (TCD), with argon (Ar) serving as the carrier gas at a flow rate of 30 mL/min.

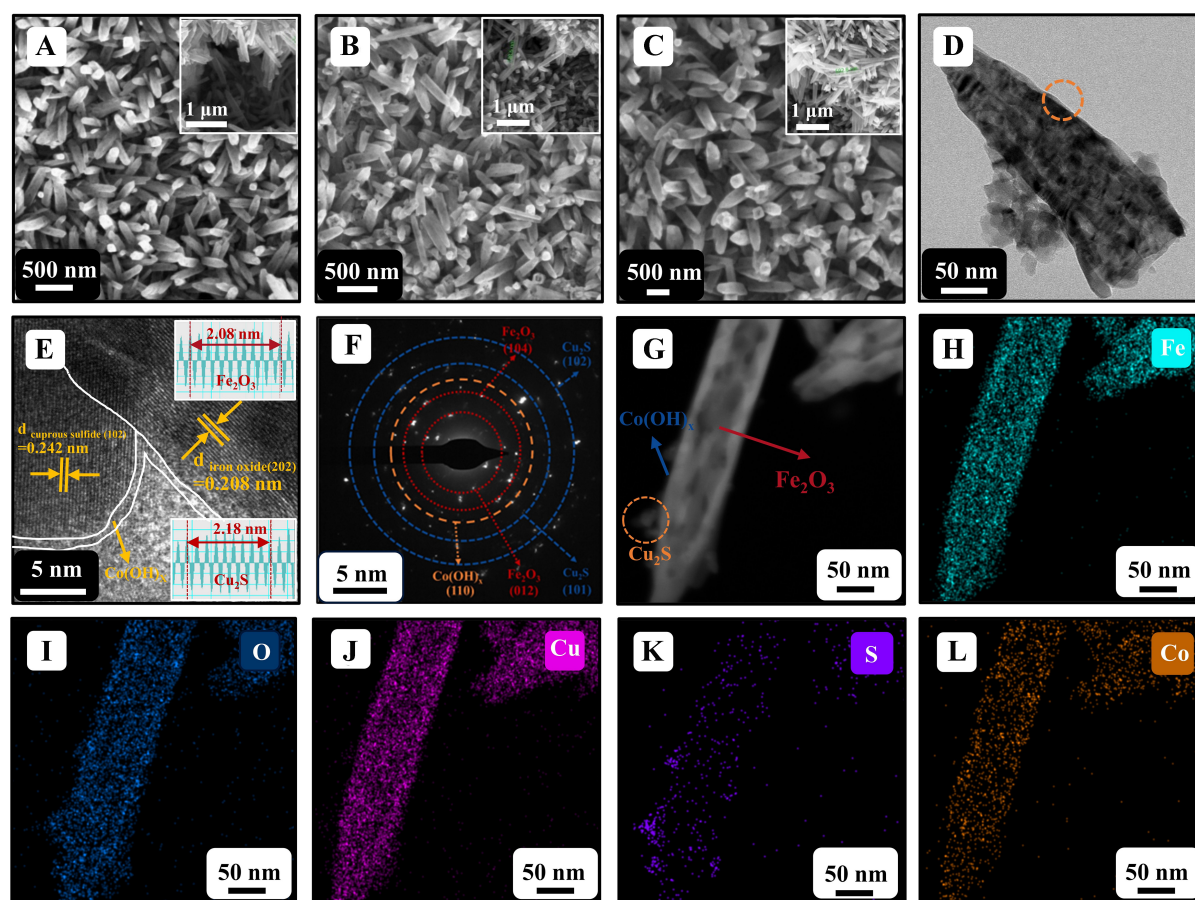


**Figure 2.** (A-C) SEM images of Ti/Fe<sub>2</sub>O<sub>3</sub>, Ti/Fe<sub>2</sub>O<sub>3</sub>/Cu<sub>2</sub>S, and Ti/Fe<sub>2</sub>O<sub>3</sub>/Cu<sub>2</sub>S/Co(OH)<sub>x</sub> photoanodes; (D and E) HRTEM images of Ti/Fe<sub>2</sub>O<sub>3</sub>/Cu<sub>2</sub>S/Co(OH)<sub>x</sub> photoanode; (F) SAED images of Ti/Fe<sub>2</sub>O<sub>3</sub>/Cu<sub>2</sub>S/Co(OH)<sub>x</sub> photoanode; (G) STEM image of Ti/Fe<sub>2</sub>O<sub>3</sub>/Cu<sub>2</sub>S/Co(OH)<sub>x</sub> photoanode; (H-L) EDS mapping (Fe, O, Cu, S and Co) of Ti/Fe<sub>2</sub>O<sub>3</sub>/Cu<sub>2</sub>S/Co(OH)<sub>x</sub> photoanode. SEM: Scanning electron microscope; HRTEM: high-resolution transmission electron microscopy; SAED: selected area electron diffraction; STEM: scanning transmission electron microscopy; EDS: energy dispersive spectroscopy.

## RESULTS AND DISCUSSION

### Morphology and structure

Ti/Fe<sub>2</sub>O<sub>3</sub>, Ti/Fe<sub>2</sub>O<sub>3</sub>/Cu<sub>2</sub>S, and Ti/Fe<sub>2</sub>O<sub>3</sub>/Cu<sub>2</sub>S/Co(OH)<sub>x</sub> photoanodes exhibit a semi-collapsed rod-shaped structure [Figure 2A-C], belonging to one-dimensional nanomaterials. The side view shows that the length of these rods is approximately 700 nm. Compared to Ti/Fe<sub>2</sub>O<sub>3</sub>, there is no obvious Cu<sub>2</sub>S and Co(OH)<sub>x</sub> on the surface of Ti/Fe<sub>2</sub>O<sub>3</sub>/Cu<sub>2</sub>S and Ti/Fe<sub>2</sub>O<sub>3</sub>/Cu<sub>2</sub>S/Co(OH)<sub>x</sub> photoanodes, which may be due to the relatively small loading amount of Cu<sub>2</sub>S and the deposition amount of Co(OH)<sub>x</sub>. By increasing the loading of Cu<sub>2</sub>S, it was demonstrated that Cu<sub>2</sub>S nanoparticles were synthesized, as detailed in Supplementary Figure 1. The rod-like structure of the Ti/Fe<sub>2</sub>O<sub>3</sub>/Cu<sub>2</sub>S/Co(OH)<sub>x</sub> photoanode is observed by TEM [Figure 2D]; in Figure 2E, the calculated lattice spacing is compared with the XRD standard spectrum, demonstrating that the (102) crystal plane of Cu<sub>2</sub>S is on the left of the figure<sup>[30]</sup>, while the (202) crystal plane of Fe<sub>2</sub>O<sub>3</sub> is on the right. In the high-resolution mode<sup>[31]</sup>, a phase interface between Fe<sub>2</sub>O<sub>3</sub> and Cu<sub>2</sub>S is observed, with a heterojunction structure forming between the two. In addition, an ultra-thin Co(OH)<sub>x</sub> film outside the Fe<sub>2</sub>O<sub>3</sub> and Cu<sub>2</sub>S heterojunction structure wraps both, forming a Co(OH)<sub>x</sub>-covered p-Cu<sub>2</sub>S/n-Fe<sub>2</sub>O<sub>3</sub> structure.

The SAED characterization results are shown in Figure 2F. The SAED profiles correspond to the (001) and (002) crystal faces in  $\text{Cu}_2\text{S}$  and (010) crystal face in  $\text{Co}(\text{OH})_x$ , which are the main peaks of  $\text{Cu}_2\text{S}$  and  $\text{Co}(\text{OH})_x$  crystals, respectively; this further proves that the presence of  $\text{Cu}_2\text{S}$  and  $\text{Co}(\text{OH})_x$  nanorods in  $\text{Ti}/\text{Fe}_2\text{O}_3/\text{Cu}_2\text{S}/\text{Co}(\text{OH})_x$  nanorods  $\text{Co}(\text{OH})_x$ . In addition, the SAED pattern corresponds to the (300) and (006) crystal faces in the  $\alpha\text{-Fe}_2\text{O}_3$  crystals, which are the main peaks of  $\alpha\text{-Fe}_2\text{O}_3$ , further proving that the main component of the  $\text{Ti}/\text{Fe}_2\text{O}_3/\text{Cu}_2\text{S}/\text{Co}(\text{OH})_x$  nanorods is  $\alpha\text{-Fe}_2\text{O}_3$ . Energy dispersive spectroscopy (EDS) surface scan characterization of the photoanode  $\text{Ti}/\text{Fe}_2\text{O}_3/\text{Cu}_2\text{S}/\text{Co}(\text{OH})_x$  [Figure 2G] was carried out. The results [Figure 2H-L] show that  $\text{Ti}/\text{Fe}_2\text{O}_3/\text{Cu}_2\text{S}/\text{Co}(\text{OH})_x$  nanorods contain both Fe, O, Cu, S, and Co, and all five elements are relatively uniformly distributed on the nanorods.

Figure 3A shows the XRD results of three types of photoanodes. By comparing them with standard cards (PDF#44-1294) and (PDF#33-0664), it is proven that they are the characteristic XRD peaks of metal Ti and  $\text{Fe}_2\text{O}_3$ . The XRD results showed that the structure of  $\text{Fe}_2\text{O}_3$  remained unchanged during the preparation and electrochemical deposition of SILAR. At the same time, no XRD peaks of  $\text{Cu}_2\text{S}$  and  $\text{Co}(\text{OH})_x$  were observed, indicating a relatively low content of  $\text{Cu}_2\text{S}$  and  $\text{Co}(\text{OH})_x$ . Additionally, the XRD fine maps of these three photoanodes from  $32.5^\circ$  to  $34.0^\circ$  [Figure 3B] reflected that the introduction of a small amount of  $\text{Cu}_2\text{S}$  and  $\text{Co}(\text{OH})_x$  did not shift the X-ray characteristic diffraction peaks of  $\text{Fe}_2\text{O}_3$  and metal Ti, which indicated that  $\text{Cu}_2\text{S}$  and  $\text{Co}(\text{OH})_x$  did not alter the physical phases of  $\text{Fe}_2\text{O}_3$  and metal Ti. They were only loaded or encapsulated on the  $\text{Fe}_2\text{O}_3$  and metal Ti.

#### Surface analysis and elemental composition

XPS was performed on  $\text{Ti}/\text{Fe}_2\text{O}_3$ ,  $\text{Ti}/\text{Fe}_2\text{O}_3/\text{Cu}_2\text{S}$ , and  $\text{Ti}/\text{Fe}_2\text{O}_3/\text{Cu}_2\text{S}/\text{Co}(\text{OH})_x$  photoanodes to confirm the formation of heterostructures and analyze the chemical states of elements. The XPS full spectrum [Figure 4A] reveals that the  $\text{Ti}/\text{Fe}_2\text{O}_3/\text{Cu}_2\text{S}/\text{Co}(\text{OH})_x$  photoanode comprises Fe, O, Cu, S, and Co. Similarly, the other two photoanodes also exhibit the presence of these elements. In the Fe 2p region [Figure 4B], the XPS spectra reveal two peaks at approximately 724 and 711 eV, characteristic of  $\text{Fe}^{3+}$ , along with two satellite peaks observed at 732.74 and 718.35 eV. It can be seen from the figure that the two main peaks at about 724 and 711 eV confirm the presence of  $\text{Fe}^{3+}$  as the main component on these three photoanodes; these main peaks are also accompanied by satellite peaks at about 733 and 718 eV, also indicative of  $\text{Fe}^{3+}$  presence; the XPS peaks of these three photoanodes show no shifts<sup>[32,33]</sup>. As can be seen from Figure 4C, the peak of the Fe–O bond of these three samples is around 529.8 eV without a significant shift. Compared to  $\text{Ti}/\text{Fe}_2\text{O}_3$ , the peaks corresponding to the high binding energy of the O element in  $\text{Ti}/\text{Fe}_2\text{O}_3/\text{Cu}_2\text{S}$  and  $\text{Ti}/\text{Fe}_2\text{O}_3/\text{Cu}_2\text{S}/\text{Co}(\text{OH})_x$  are shifted towards higher binding energies, attributed to the formation of S–O bonds<sup>[20]</sup>. In the Cu 2p spectrum [Figure 4D], the peaks observed at 951.90 and 932.03 eV correspond well to  $\text{Cu } 2p^{1/2}$  and  $\text{Cu } 2p^{3/2}$  of  $\text{Cu}^+$ . Additionally, the absence of the characteristic jitter peak between the  $\text{Cu } 2p^{1/2}$  and  $2p^{3/2}$  peaks suggests the absence of  $\text{Cu}^{2+}$ <sup>[34,35]</sup>. Consistent with the findings in the Cu 2p spectrum, the presence of two peaks at S  $2p^{1/2}$  (163.4 eV) and S  $2p^{3/2}$  (162.3 eV) [Figure 4E] confirms the formation of  $\text{Cu}_2\text{S}$ <sup>[20]</sup>. Compared with  $\text{Ti}/\text{Fe}_2\text{O}_3$ , a pair of weak peaks were observed at 164.3 and 162.3 eV for the as-prepared  $\text{Ti}/\text{Fe}_2\text{O}_3/\text{Cu}_2\text{S}$  and  $\text{Ti}/\text{Fe}_2\text{O}_3/\text{Cu}_2\text{S}/\text{Co}(\text{OH})_x$  photoanodes, which were assigned to  $\text{Cu}_2\text{S}$ . The S–O bond between  $\text{Fe}_2\text{O}_3$  is completely consistent with previous reports<sup>[36,37]</sup>. The Co 2p spectrum [Figure 4F] also shows two main peaks near 781 eV (corresponding to  $\text{Co } 2p^{3/2}$ ), and a dithered satellite peak (near 786 eV), which corresponds to  $\text{Co}^{3+}$  and  $\text{Co}^{2+}$ , respectively<sup>[38,39]</sup>. The fitting results show that the content of  $\text{Co}^{3+}$  in the composite is relatively higher than that of  $\text{Co}^{2+}$ , which is beneficial for obtaining excellent catalytic activity<sup>[38]</sup>. In addition, a satellite peak located near 786 eV can be attributed to the Co hydroxyl group<sup>[40]</sup>. The formation of Co hydroxyl groups will have a positive impact on the OER performance, as it may induce structural flexibility and an optimized coordination state<sup>[41]</sup>.

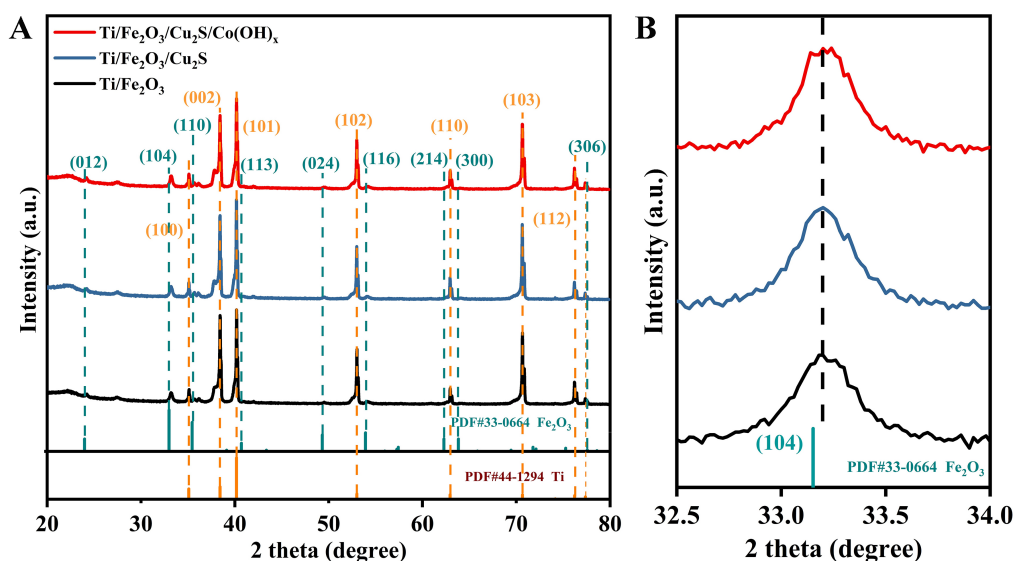


**Figure 3.** (A) XRD patterns of  $\text{Ti/Fe}_2\text{O}_3$ ,  $\text{Ti/Fe}_2\text{O}_3/\text{Cu}_2\text{S}$ , and  $\text{Ti/Fe}_2\text{O}_3/\text{Cu}_2\text{S/Co(OH)}_x$  photoanodes; (B) XRD fine patterns of  $\text{Ti/Fe}_2\text{O}_3$ ,  $\text{Ti/Fe}_2\text{O}_3/\text{Cu}_2\text{S}$ , and  $\text{Ti/Fe}_2\text{O}_3/\text{Cu}_2\text{S/Co(OH)}_x$  photoanodes. XRD: X-ray diffraction.

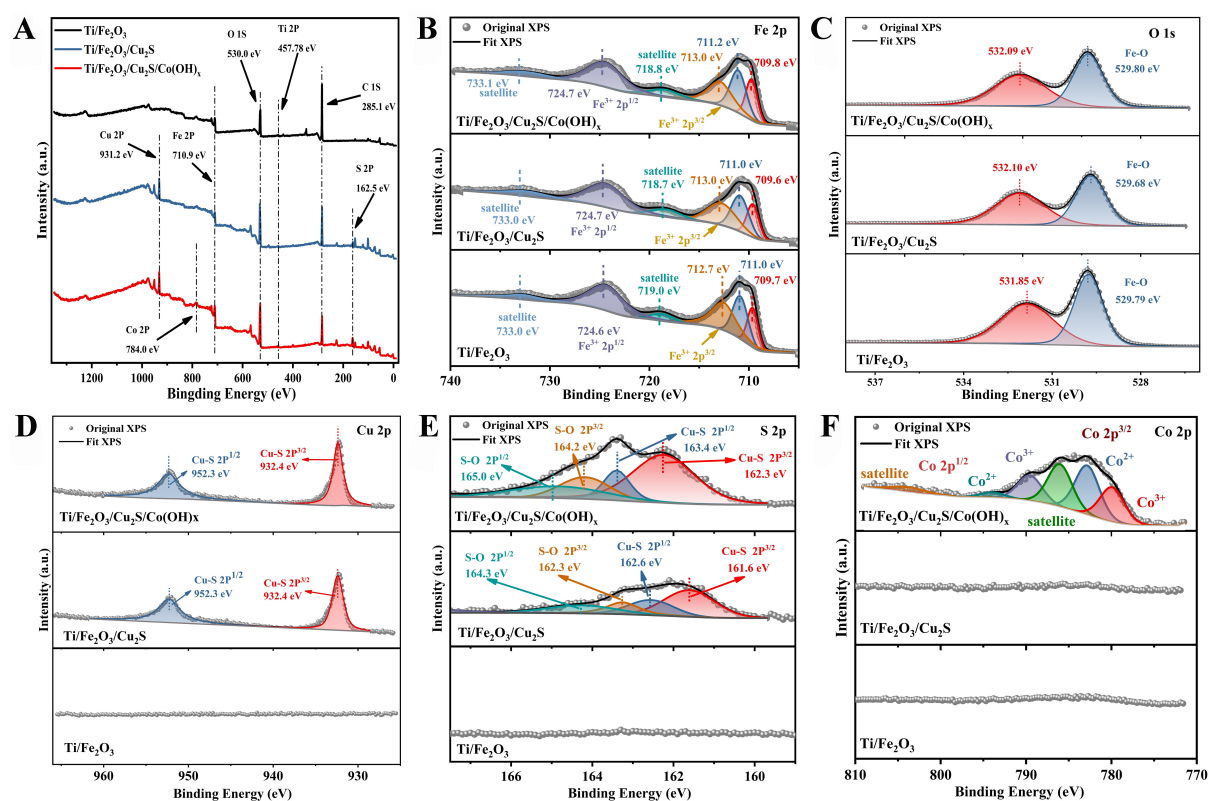


**Figure 4.** XPS spectra of  $\text{Ti/Fe}_2\text{O}_3$ ,  $\text{Ti/Fe}_2\text{O}_3/\text{Cu}_2\text{S}$ , and  $\text{Ti/Fe}_2\text{O}_3/\text{Cu}_2\text{S/Co(OH)}_x$  photoanodes. (A) the survey spectra; (B) Fe 2p; (C) O 1s; (D) Cu 2p; (E) S 2p; and (F) Co 2p. XPS: X-ray photoelectron spectroscopy.

As shown in Figure 5A, the trend of the curves of the UV-vis absorption spectra of these three photoanodes is consistent, and the test results illustrate that the absorption of these three samples is relatively strong in

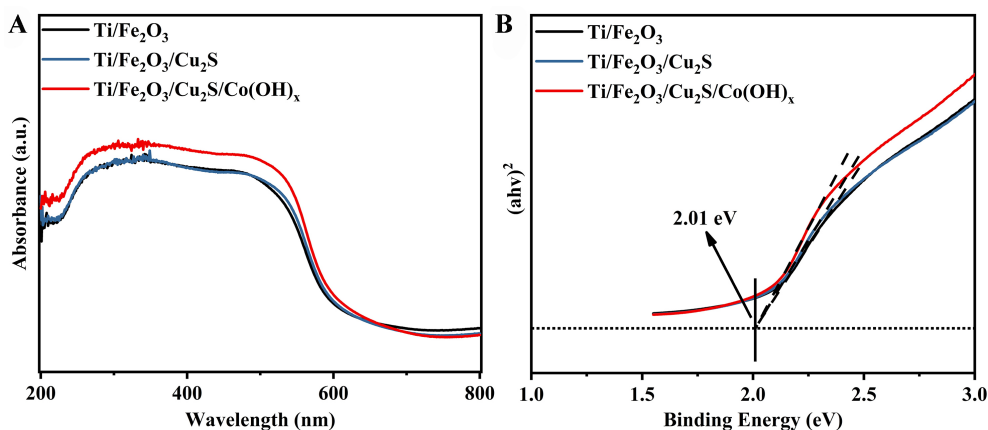


**Figure 5.** (A) UV-Vis absorption spectra of Ti/Fe<sub>2</sub>O<sub>3</sub>, Ti/Fe<sub>2</sub>O<sub>3</sub>/Cu<sub>2</sub>S, and Ti/Fe<sub>2</sub>O<sub>3</sub>/Cu<sub>2</sub>S/Co(OH)<sub>x</sub> photoanodes; (B) The bandgap diagram of Ti/Fe<sub>2</sub>O<sub>3</sub>, Ti/Fe<sub>2</sub>O<sub>3</sub>/Cu<sub>2</sub>S, and Ti/Fe<sub>2</sub>O<sub>3</sub>/Cu<sub>2</sub>S/Co(OH)<sub>x</sub> photoanodes. UV-Vis: Ultraviolet-visible.

the UV region and in the visible region from 420 to 600 nm. The bandgap can be estimated from the Tauc plot [Equation (1)]<sup>[42]</sup>, so that the bandgap of Fe<sub>2</sub>O<sub>3</sub>, the main semiconductor material of the three photoanodes, can be deduced from the test results of the UV-Vis diffuse reflectance spectra to be 1.98 eV [Figure 5B].

## PEC and EC analysis

### PEC measurement

A series of PEC tests<sup>[43]</sup> were used to characterize the iron oxide nanorod photoanode<sup>[44]</sup>. The LSV results [Figure 6A] indicate the photocurrent performance of different samples in a 1 M KOH electrolyte solution at potentials ranging from 0.7 (vs. RHE) to 1.6 V (vs. RHE). Under AM 1.5G irradiation, as P-type Cu<sub>2</sub>S semiconductors and ultra-thin Co(OH)<sub>x</sub> nanosheets were gradually introduced, the photocurrent density of the photoanode significantly increased. The Ti/Fe<sub>2</sub>O<sub>3</sub>/Cu<sub>2</sub>S/Co(OH)<sub>x</sub> photoanode showed the highest photocurrent density, about 4.81 mA/cm<sup>2</sup> at 1.23 V (vs. RHE), which was about three times that of the original Ti/Fe<sub>2</sub>O<sub>3</sub> (1.62 mA/cm<sup>2</sup>). Under visible light irradiation (Figure 6B, λ > 420 nm, 66.7 mW/cm<sup>2</sup>), the photocurrent density of the Ti/Fe<sub>2</sub>O<sub>3</sub>/Cu<sub>2</sub>S/Co(OH)<sub>x</sub> photoanode is about half of that under AM 1.5G irradiation, measuring about 2.39 mA/cm<sup>2</sup> at 1.23 V (vs. RHE). This indicates good visible photocatalytic activity. We also explored the advantages of one-dimensional morphology in observing high photocurrents [Supplementary Figure 2]. In addition, different Cu<sub>2</sub>S and Co(OH)<sub>x</sub> contents affect the PEC characteristics of Ti/Fe<sub>2</sub>O<sub>3</sub> [Supplementary Figure 3].

Supplementary Table 1 shows the PEC performance of the Ti/Fe<sub>2</sub>O<sub>3</sub>/Cu<sub>2</sub>S/Co(OH)<sub>x</sub> photoanodes in this study compared to other recently reported Fe<sub>2</sub>O<sub>3</sub>-based photoanodes. The final comparison results show the excellent performance of our prepared photoanode.

The ABPE [Figure 6C] of each photoanode below the water oxidation thermodynamic potential (1.23 V vs. RHE) was calculated based on the LSV results<sup>[45]</sup>. Figure 6C illustrates that the ABPE efficiency of the Ti/Fe<sub>2</sub>O<sub>3</sub>/Cu<sub>2</sub>S/Co(OH)<sub>x</sub> photoanode was significantly enhanced compared with Ti/Fe<sub>2</sub>O<sub>3</sub>, Ti/Fe<sub>2</sub>O<sub>3</sub>/Cu<sub>2</sub>S, and Ti/Fe<sub>2</sub>O<sub>3</sub>/Co(OH)<sub>x</sub>. At 1.03 V (vs. RHE), it reached 0.48%, which is 3.2 times higher than that of the Ti/Fe<sub>2</sub>O<sub>3</sub> photoanode (0.15%, 1.03 V vs. RHE). Furthermore, under visible light irradiation (λ > 420 nm, light intensity 66.7 mW/cm<sup>2</sup>, Figure 6D), the Ti/Fe<sub>2</sub>O<sub>3</sub>/Cu<sub>2</sub>S/Co(OH)<sub>x</sub> photoanode exhibited the highest ABPE of 0.2%.

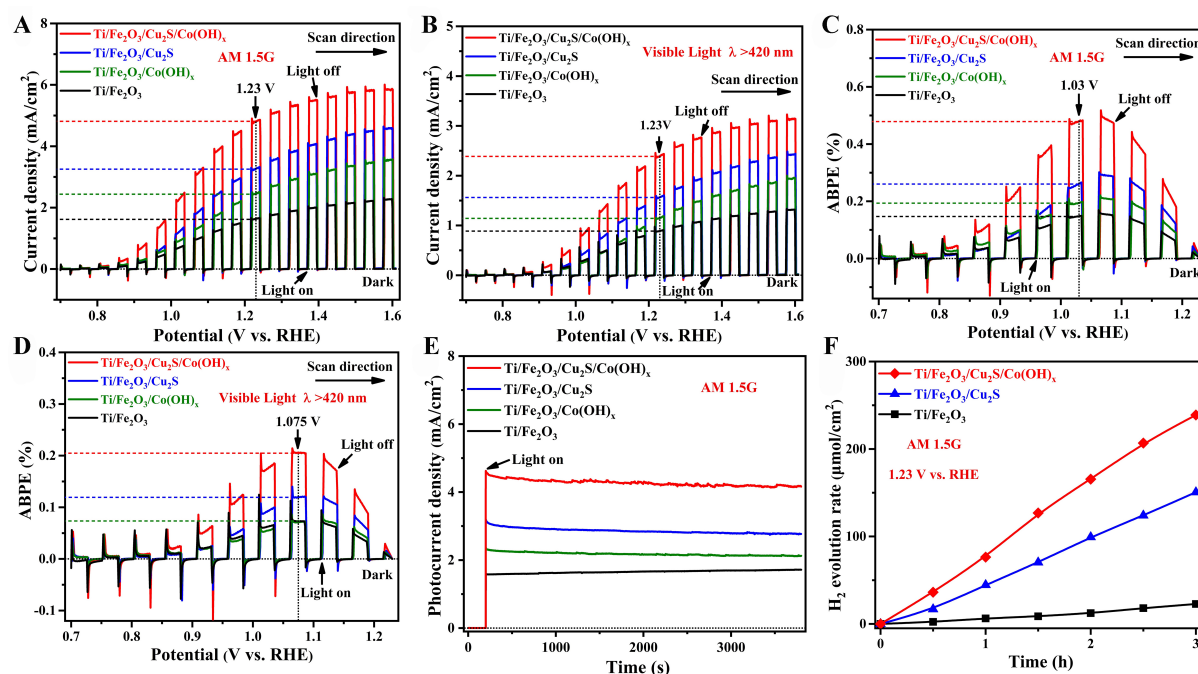


**Figure 6.** PEC performance of  $\text{Ti/Fe}_2\text{O}_3$ ,  $\text{Ti/Fe}_2\text{O}_3/\text{Cu}_2\text{S}$ , and  $\text{Ti/Fe}_2\text{O}_3/\text{Cu}_2\text{S}/\text{Co(OH)}_x$  photoanodes. (A) Chopped LSV curves under AM 1.5G (100 mW/cm<sup>2</sup>); (B) Chopped LSV curves under visible light ( $\lambda > 420$  nm, 66.7 mW/cm<sup>2</sup>); (C) ABPE curves under AM 1.5G (100 mW/cm<sup>2</sup>); (D) ABPE curves under visible light irradiation ( $\lambda > 420$  nm, 66.7 mW/cm<sup>2</sup>); (E) I-t data plots at 1.23 V vs. RHE; (F) PEC H<sub>2</sub> evolution across different samples at 1.23 V vs. RHE. PEC: Photoelectrochemical; LSV: linear sweep voltammetry; ABPE: applied bias photon-to-current efficiency; RHE: reversible hydrogen electrode.

#### I-t and measurement of light-assisted H<sub>2</sub> production

To verify the stability of the prepared photoanode, chronoamperometry (I-t) was conducted [Figure 6E]. Under continuous illumination for 1 h, the  $\text{Ti/Fe}_2\text{O}_3/\text{Cu}_2\text{S}/\text{Co(OH)}_x$  (I-t, 1.23 V vs. RHE) photoanode showed good stability, and the photocurrent remained almost unchanged. To further demonstrate the stability of the synthesized samples, a 19-hour stability test [Supplementary Figure 4] was performed on top of the original 1-hour test [Figure 6E]. The results indicated that the samples exhibited enhanced stability. Following the stability tests, the samples were subjected to a series of characterizations [Supplementary Figures 5-11].

The actual H<sub>2</sub> generation performance of various samples at 1.23 V (vs. RHE) was recorded to investigate the relevance of the observation of photocurrent to the solar-assisted hydrolysis H<sub>2</sub> generation reaction. Photoanodes with high photocurrent density often exhibit higher hydrogen production rates under optoelectronic conditions. The 3-hour measurement period [Figure 6F] showed a linear increase in the amount of H<sub>2</sub> generation over time, indicating a stable H<sub>2</sub> generation rate for the sample and reaffirming the stability of the  $\text{Ti/Fe}_2\text{O}_3/\text{Cu}_2\text{S}/\text{Co(OH)}_x$  photoanode.

#### IPCE measurement

In order to explore the response of the photoanode to different wavelengths of light, the prepared photoanode was used to conduct the IPCE test. During the test, the light source irradiates from 300 nm, changes to 600 nm at a constant speed, and ends at 600 nm; the wavelength resolution of the spectral analysis is 1 nm. It can be seen from Figure 7A that under the electrochemical noise mode, the pristine  $\text{Ti/Fe}_2\text{O}_3$  photoanode has photocurrent performance in the wavelength region of 300-600 nm, which indicates that  $\text{Fe}_2\text{O}_3$  material has a wide light absorption range and an excellent visible light response.

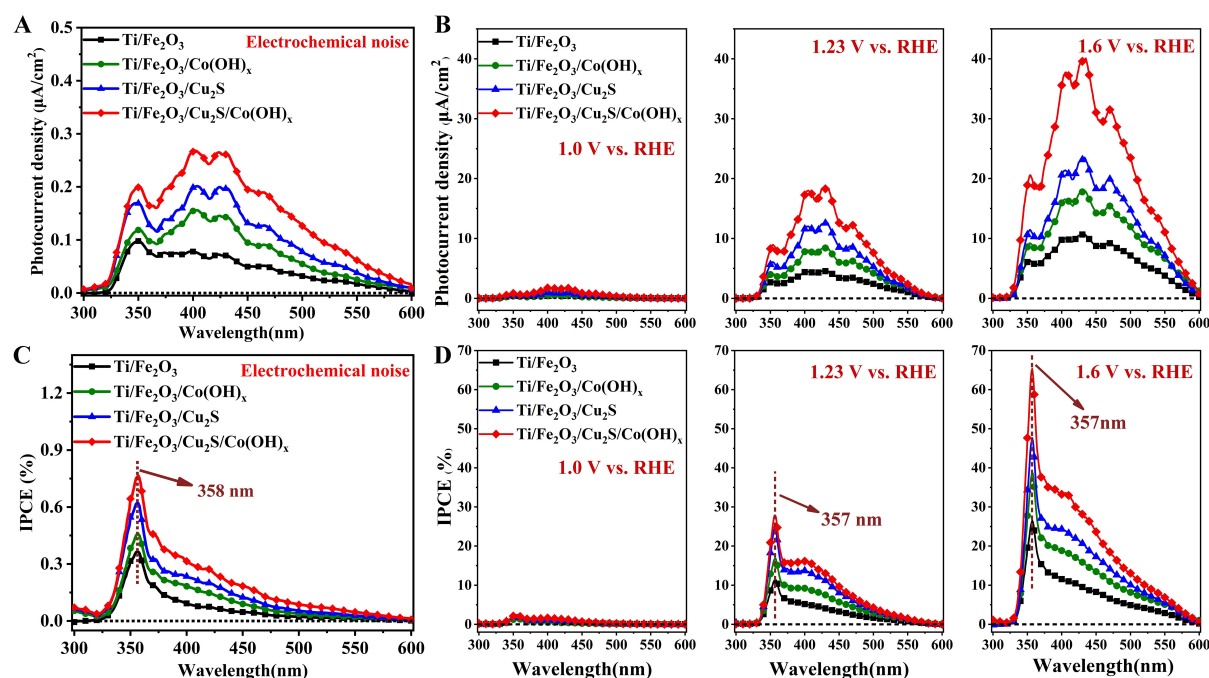


**Figure 7.** (A and B) Photocurrent density vs. the monochromatic light; (C and D) Derived IPCE (%) spectra of samples under different bias. IPCE: Incident monochromatic photon electron conversion efficiency.

Compared with  $\text{Ti/Fe}_2\text{O}_3$ , the photocurrent densities and IPCE values of  $\text{Ti/Fe}_2\text{O}_3/\text{Cu}_2\text{S}$ ,  $\text{Ti/Fe}_2\text{O}_3/\text{Co(OH)}_x$ , and  $\text{Ti/Fe}_2\text{O}_3/\text{Cu}_2\text{S/Co(OH)}_x$  photoanodes gradually increase, which shows that the introduction of  $\text{Cu}_2\text{S}$  and  $\text{Co(OH)}_x$  improves the photoelectric performance of  $\text{Fe}_2\text{O}_3$ ; this improvement covers the entire wavelength range from 300 to 600 nm. Under the constant potential polarization mode with different applied bias voltages [Figure 7B], the photocurrent density and IPCE value of these photoanodes gradually increase with higher bias voltages, which shows that increasing the applied bias voltage is helpful for photogenerated current carrying. The separation of electrons strengthens the photoelectric properties of the sample. Under the conditions of the electrochemical noise test [Figure 7C] and constant potential test [Figure 7D], the IPCE peaks of  $\text{Ti/Fe}_2\text{O}_3$ ,  $\text{Ti/Fe}_2\text{O}_3/\text{Cu}_2\text{S}$ ,  $\text{Ti/Fe}_2\text{O}_3/\text{Co(OH)}_x$ , and  $\text{Ti/Fe}_2\text{O}_3/\text{Cu}_2\text{S/Co(OH)}_x$  photoanodes are all at 357 nm place. Under electrochemical noise test conditions, at 1.23 (vs. RHE) and 1.6 V (vs. RHE), the peak IPCE values of the  $\text{Ti/Fe}_2\text{O}_3/\text{Cu}_2\text{S/Co(OH)}_x$  photoanode are 0.76%, 27.6%, and 64.7%, respectively.

### MS analysis

To investigate the energy band structure information of the  $\text{Ti/Fe}_2\text{O}_3/\text{Cu}_2\text{S/Co(OH)}_x$  photoanode, key parameters such as the conduction band (CB), flat band potential, and carrier concentration were determined. The effects of the introduction of  $\text{Cu}_2\text{S}$  and  $\text{Co(OH)}_x$  on the  $\text{Ti/Fe}_2\text{O}_3$  photoanode were also examined. Therefore,  $\text{Ti/Fe}_2\text{O}_3$ ,  $\text{Ti/Fe}_2\text{O}_3/\text{Cu}_2\text{S}$ ,  $\text{Ti/Fe}_2\text{O}_3/\text{Co(OH)}_x$  and  $\text{Ti/Fe}_2\text{O}_3/\text{Cu}_2\text{S/Co(OH)}_x$  photoanodes were all subjected to MS tests.

The longest segment of the MS curve makes an extension line to get the intersection with the baseline for the flat-charged potential position. The intersection of the extension lines for the different frequencies of the four photoanodes is a single point<sup>[46]</sup>. The positive slopes of the tangent lines for all four samples indicate their n-type nature<sup>[20]</sup>. In both n- and p-type semiconductors, the flat band potential can be approximated as the CB potential. The results shown in Figure 8A-D indicate that the introduction of both  $\text{Cu}_2\text{S}$  and

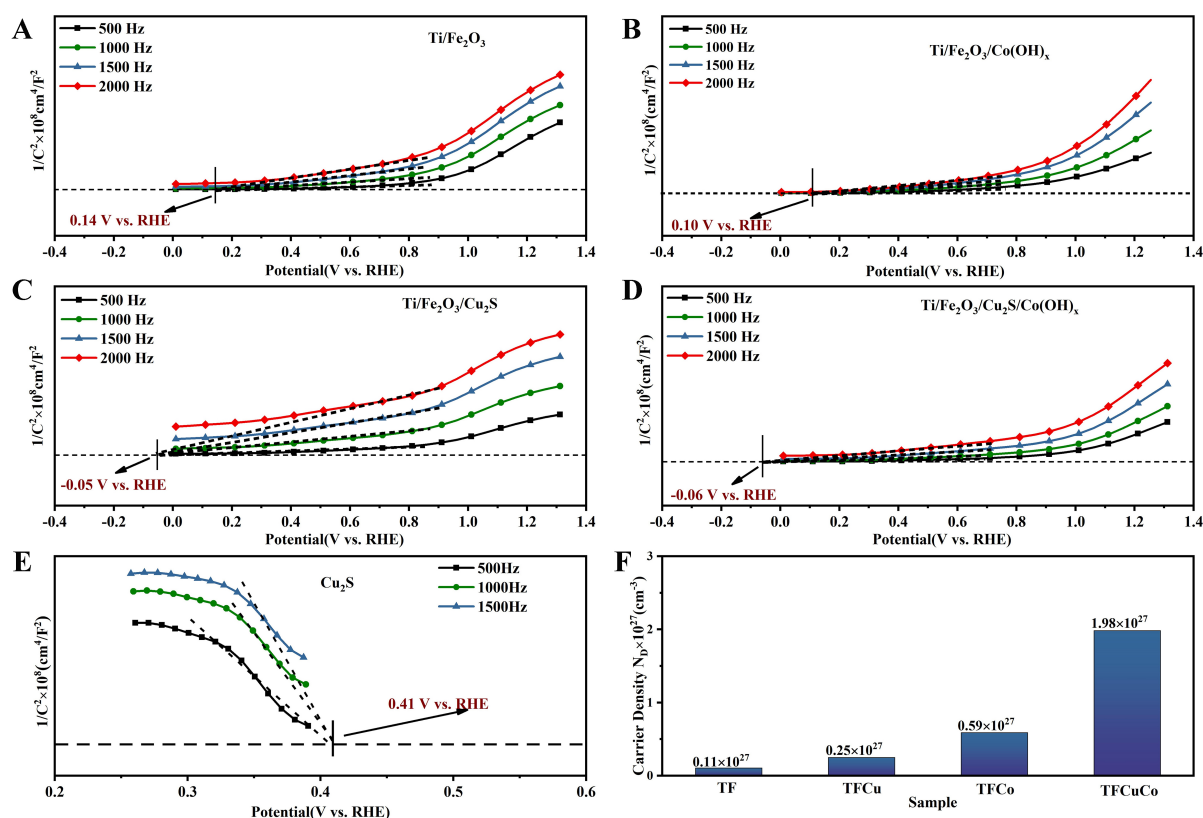


**Figure 8.** Mott-Schottky plots have frequencies from 500 to 2,000 Hz. (A)  $\text{Ti/Fe}_2\text{O}_3$  photoanode; (B)  $\text{Ti/Fe}_2\text{O}_3/\text{Cu}_2\text{S}$  photoanode; (C)  $\text{Ti/Fe}_2\text{O}_3/\text{Co(OH)}_x$  photoanode; (D)  $\text{Ti/Fe}_2\text{O}_3/\text{Cu}_2\text{S}/\text{Co(OH)}_x$  photoanode; (E) Frequency (500 to 1,500 Hz) of the Mott-Schottky diagram of  $\text{Cu}_2\text{S}$  nanoparticles; (F) The carrier concentrations of  $\text{Ti/Fe}_2\text{O}_3$  photoanode (TF),  $\text{Ti/Fe}_2\text{O}_3/\text{Cu}_2\text{S}$  photoanode (TFCu),  $\text{Ti/Fe}_2\text{O}_3/\text{Co(OH)}_x$  photoanode (TFCo), and  $\text{Ti/Fe}_2\text{O}_3/\text{Cu}_2\text{S}/\text{Co(OH)}_x$  photoanode (TFCuCo).

$\text{Co(OH)}_x$  results in a more negative flat-band potential for the  $\text{Ti/Fe}_2\text{O}_3$  photoanode. Compared to the  $\text{Ti/Fe}_2\text{O}_3$  photoanode, the CB potential of the  $\text{Ti/Fe}_2\text{O}_3/\text{Co(OH)}_x$ ,  $\text{Ti/Fe}_2\text{O}_3/\text{Cu}_2\text{S}$ , and  $\text{Ti/Fe}_2\text{O}_3/\text{Cu}_2\text{S}/\text{Co(OH)}_x$  photoanodes were reduced from 0.14 (vs. RHE for  $\text{Ti/Fe}_2\text{O}_3$ ) to 0.10, -0.05, and -0.06 V (vs. RHE), respectively. A negative movement of the flat band potential suggests a reduced energy potential barrier for electron transfer at the interface, contributing to a reduction in the charge transfer resistance<sup>[44]</sup>. Therefore, compared with the other three, the  $\text{Ti/Fe}_2\text{O}_3/\text{Cu}_2\text{S}/\text{Co(OH)}_x$  photoanode has the most negative CB potential and the best photocurrent and photocoupling hydrogen production performance, corresponding to the previous results.

Separately synthesized  $\text{Cu}_2\text{S}$  powders were also tested for MS; the results are shown in Figure 8E. The intersection of the extension lines of the data curves for the three different frequencies is a point whose tangent line has a negative slope, which reveals that the  $\text{Cu}_2\text{S}$  semiconductor has p-type properties<sup>[47]</sup> with a flat-band potential (approximated as the conduction-band potential) of 0.14 V (vs. RHE). The carrier concentrations of these four photoanodes were calculated from the MS test data [Figure 8F]. The results show that the carrier concentration of the  $\text{Ti/Fe}_2\text{O}_3/\text{Cu}_2\text{S}/\text{Co(OH)}_x$  photoanode is one magnitude higher compared with that of the  $\text{Ti/Fe}_2\text{O}_3$ ,  $\text{Ti/Fe}_2\text{O}_3/\text{Cu}_2\text{S}$ , and  $\text{Ti/Fe}_2\text{O}_3/\text{Co(OH)}_x$ , which is one of the reasons for its good performance.

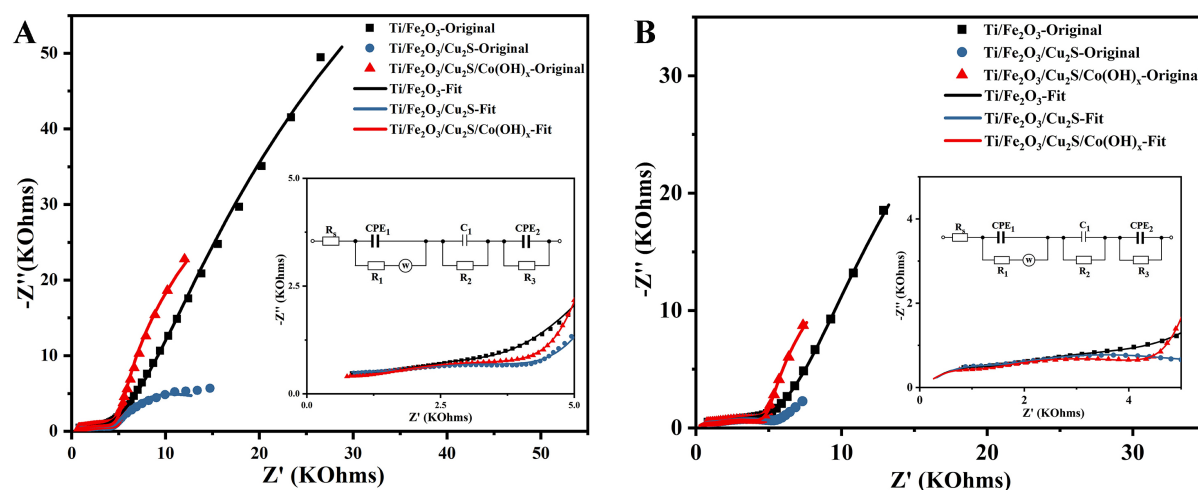


**Figure 9.** EIS and Equivalent Circuit of Ti/Fe<sub>2</sub>O<sub>3</sub> photoanode, Ti/Fe<sub>2</sub>O<sub>3</sub>/Cu<sub>2</sub>S photoanode and Ti/Fe<sub>2</sub>O<sub>3</sub>/Cu<sub>2</sub>S/Co(OH)<sub>x</sub> photoanode at (A) 1.23 V vs. RHE and at (B) OCP. EIS: Electrochemical impedance spectroscopy; RHE: reversible hydrogen electrode; OCP: open circuit potential.

### EIS analysis

Frequency transmission characteristics and electrochemical properties of photoanodes were studied using EIS<sup>[48]</sup>. Nyquist plots were obtained for the samples under dark conditions at open-circuit potential [Figure 9A] and at 1.23 V (vs. RHE) [Figure 9B]. Measurements were conducted in the frequency range of 100 MHz to 100 kHz. The equivalent circuit [Figure 9] includes a resistor (R), a capacitor (C), a constant phase element (CPE), and a Warburg impedance element (W). From the small figure in Figure 9A, it can be seen (under open-circuit potential conditions) that the radii of the arcs of the EIS curves are smaller than those of Ti/Fe<sub>2</sub>O<sub>3</sub>/Cu<sub>2</sub>S and Ti/Fe<sub>2</sub>O<sub>3</sub>/Cu<sub>2</sub>S/Co(OH)<sub>x</sub> in the high-frequency region (0-5 KOhms); moreover, from the internal small figure in Figure 9B, it can be seen that the radii of the arcs of the EIS curves are smaller than those of Ti/Fe<sub>2</sub>O<sub>3</sub> and Ti/Fe<sub>2</sub>O<sub>3</sub>/Cu<sub>2</sub>S/Co(OH)<sub>x</sub> in the high-frequency region (0-5 KOhms). Specifically, the arc radius of the EIS curve for Ti/Fe<sub>2</sub>O<sub>3</sub>/Cu<sub>2</sub>S/Co(OH)<sub>x</sub> is smaller than that of both Ti/Fe<sub>2</sub>O<sub>3</sub> and Ti/Fe<sub>2</sub>O<sub>3</sub>/Cu<sub>2</sub>S. A lower arc radius means a lower charge transfer resistance in the electrode, facilitating rapid separation and transfer of photogenerated carriers<sup>[49]</sup>. The fitted data for the curves measured at 1.23 V (vs. RHE) are presented in Supplementary Table 2, and these values are significantly lower for Ti/Fe<sub>2</sub>O<sub>3</sub>/Cu<sub>2</sub>S and Ti/Fe<sub>2</sub>O<sub>3</sub>/Cu<sub>2</sub>S/Co(OH)<sub>x</sub> compared with R<sub>s</sub>, R<sub>2</sub>, R<sub>3</sub>, and Z<sub>w</sub> for Ti/Fe<sub>2</sub>O<sub>3</sub>, which are also in the same order of magnitude with little difference in R<sub>1</sub><sup>[44]</sup>. The capacitance of the electrode bilayers C<sub>1</sub> and CPE<sub>2</sub> is also improved significantly, and these three CPE<sub>1</sub> are also in the same order of magnitude with little difference. The value of R<sub>2</sub> decreases significantly from 140 KΩ for Ti/Fe<sub>2</sub>O<sub>3</sub> to 6.07 KΩ for Ti/Fe<sub>2</sub>O<sub>3</sub>/Cu<sub>2</sub>S, and R<sub>3</sub> reduces from 1,220 Ω for Ti/Fe<sub>2</sub>O<sub>3</sub> to 509 Ω for Ti/Fe<sub>2</sub>O<sub>3</sub>/Cu<sub>2</sub>S/Co(OH)<sub>x</sub> of 509 Ω. In addition, the fitted data for the curves measured at open-circuit potentials [Supplementary Table 3] reflect the same trend. These results indicate that introducing P-type Cu<sub>2</sub>S nanoparticle semiconductors and electrodeposition of an ultrathin layer of Co(OH)<sub>x</sub> improved the charge transport of iron oxide and promoted the surface photogenerated carrier separation and transfer.  $\eta_{\text{surface}}$  curves prove it even further [Supplementary Figure 12].

### Mechanistic analysis and bandgap calculation

The  $E_g$  of the photoanode samples are calculated using Tauc plots, which depict  $[(\text{IPCE}\% \times h\nu)^{1/2}]$  against photon energy ( $h\nu$ ) in the electrochemical noise mode<sup>[44]</sup> [Figure 10A]. The main component of all four photoanodes is  $\alpha$ -Fe<sub>2</sub>O<sub>3</sub>, so they all reflect the  $E_g$  of  $\alpha$ -Fe<sub>2</sub>O<sub>3</sub> of 2.10 eV, which agrees with the previously reported results<sup>[50]</sup>. The  $E_g$  can be evaluated from the Tauc plot [Equation (1)]. The  $E_g$  [Figure 10B] of the

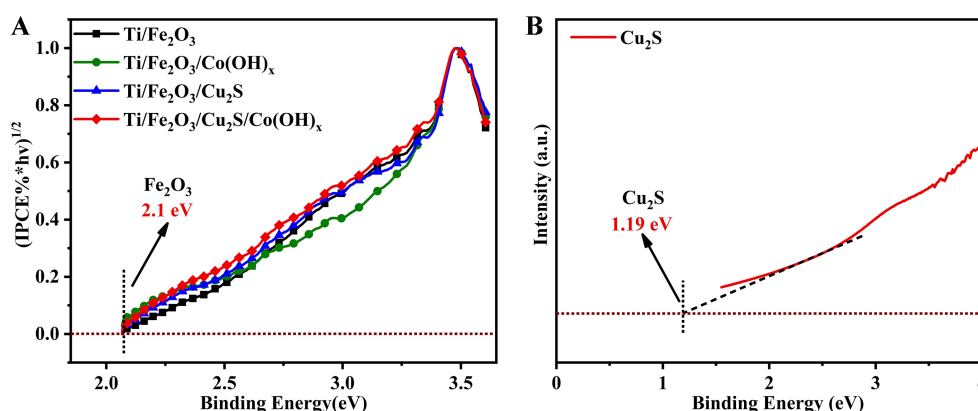


**Figure 10.** (A) The bandgap energy ( $E_g$ ) of  $\text{Ti}/\text{Fe}_2\text{O}_3$  photoanode,  $\text{Ti}/\text{Fe}_2\text{O}_3/\text{Cu}_2\text{S}$  photoanode,  $\text{Ti}/\text{Fe}_2\text{O}_3/\text{Co}(\text{OH})_x$  photoanode and  $\text{Ti}/\text{Fe}_2\text{O}_3/\text{Cu}_2\text{S}/\text{Co}(\text{OH})_x$  photoanode calculated through IPCE testing; (B) The bandgap energy ( $E_g$ ) of  $\text{Cu}_2\text{S}$  nanoparticles calculated through UV-vis-DRS testing. IPCE: incident monochromatic photon electron conversion efficiency; UV-vis-DRS: ultraviolet-visible diffuse reflectance spectroscopy.

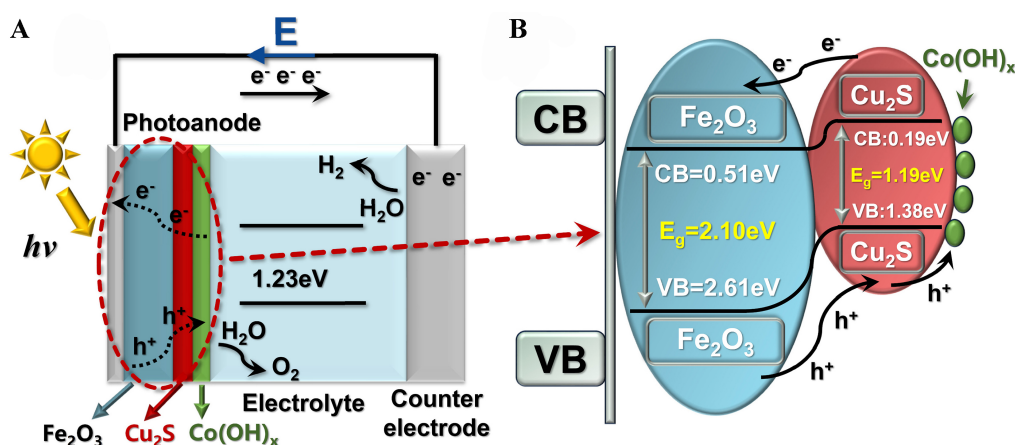


**Figure 11.** (A) Photoanode  $\text{Ti}/\text{Fe}_2\text{O}_3/\text{Cu}_2\text{S}/\text{Co}(\text{OH})_x$  photoelectric hydrogen production mechanism diagram; (B) Photoanode  $\text{Ti}/\text{Fe}_2\text{O}_3/\text{Cu}_2\text{S}/\text{Co}(\text{OH})_x$  energy band gap diagram.

$\text{Cu}_2\text{S}$  semiconductor nanoparticles alone was calculated by UV-vis spectroscopy test as 1.19 eV.

Figure 11A and B shows the  $E_g$  structure map based on the IPCE electrochemical noise pattern, UV-vis spectroscopy, and MS measurements. The valence band (VB) of the photocatalytic sample is determined from the estimated CB and  $E_g$ . Results indicate that the VB and CB of n- $\text{Fe}_2\text{O}_3$  are 2.24 and 0.14 V, respectively, while those of p- $\text{Cu}_2\text{S}$  are 0.41 and 0.14 V, respectively.

By the observations of the above experiments, we present the charge separation mechanism of ultra-thin  $\text{Co}(\text{OH})_x$  package p- $\text{Cu}_2\text{S}/\text{n-Fe}_2\text{O}_3$  to explain its strengthened PEC properties [Figure 9]<sup>[19,51]</sup>. Before contact, the CB and VB energy levels of p-type  $\text{Cu}_2\text{S}$  are higher than those of n-type  $\text{Fe}_2\text{O}_3$ , whereas the Fermi energy level (EF) of  $\text{Cu}_2\text{S}$  is lower than that of  $\text{Fe}_2\text{O}_3$ . After forming the p-n junction heterostructure, the energy level of  $\text{Cu}_2\text{S}$  rises while that of  $\text{Fe}_2\text{O}_3$  decreases, leading to an equilibrium of their EFs. Consequently, an internal electric field is formed at the  $\text{Fe}_2\text{O}_3/\text{Cu}_2\text{S}$  interface under thermodynamic equilibrium conditions. Due to the energy matching between  $\text{Fe}_2\text{O}_3$  and  $\text{Cu}_2\text{S}$ , their energy bands shift together until the Fermi levels align, resulting in band bending in the space charge region. Electrons generated and separated in the CB of

Cu<sub>2</sub>S move to the CB of Fe<sub>2</sub>O<sub>3</sub>, while holes separated and retained in the VB of Fe<sub>2</sub>O<sub>3</sub> flow to the VB of Cu<sub>2</sub>S to react with the electrolyte. Therefore, the p-Cu<sub>2</sub>S/n-Fe<sub>2</sub>O<sub>3</sub> heterojunction photoanode enhances photogenerated electron-hole pair separation and improves light harvesting efficiency. After modification with the Co(OH)<sub>x</sub> co-catalyst on Fe<sub>2</sub>O<sub>3</sub>/Cu<sub>2</sub>S, photogenerated electrons are efficiently transferred from Fe<sub>2</sub>O<sub>3</sub>/Cu<sub>2</sub>S to the Pt electrode with high electron mobility. Meanwhile, holes migrating to the surface or subsurface are captured by the outermost Co(OH)<sub>x</sub> catalyst and react with the electrolyte, increasing hole mobility and optimizing the kinetics of hole-mediated water oxidation.

## CONCLUSIONS

In conclusion, we synthesized an ultrathin Co(OH)<sub>x</sub>-encapsulated p-Cu<sub>2</sub>S/n-Fe<sub>2</sub>O<sub>3</sub>, which enhances charge separation and surface oxygen evolution kinetics of the iron oxide nanorod array photoanode through the synergistic effect of p-n heterojunctions and OECs. In 1 M KOH solution [25 °C, AM 1.5G, 1.23 V (vs. RHE)], the photocurrent density of Ti/Fe<sub>2</sub>O<sub>3</sub>/Cu<sub>2</sub>S/Co(OH)<sub>x</sub> is about three times that of Ti/Fe<sub>2</sub>O<sub>3</sub>, reaching 4.8 mA/cm<sup>2</sup>. Under visible light irradiation [ $\lambda > 420$  nm, AM 1.5G, 1.23 V (vs. RHE)], its photocurrent density also reaches 2.4 mA/cm<sup>2</sup>, which is half of the full spectrum light; in addition, the corresponding optical response limit is extended to 600 nm. Without sacrificial agents and photosensitizers, we observed a significant increase in the hydrogen evolution rate of Ti/Fe<sub>2</sub>O<sub>3</sub>/Cu<sub>2</sub>S/Co(OH)<sub>x</sub>, reaching 76.4  $\mu$ mol/cm<sup>2</sup>. Our work provides a novel concept for photoanode PEC water splitting.

## DECLARATIONS

### Authors' contributions

Prepared and revised the manuscript: Shi HY, Ji MH, Zhou QQ, Li KX, Wang HL, Chen R

Designed and revised the manuscript: Chen YX, Lin XM, Lu CZ

All authors contributed to the discussion and preparation of the manuscript.

### Availability of data and materials

The authors confirm that the data supporting the findings of this study are available within its [Supplementary Materials](#).

### Financial support and sponsorship

Authors are thankful for the financial support of the Natural Science Foundation of Fujian Province (2023H0046), the XMIREM autonomously deployment project (2023CX10, 2023GG01), the National Natural Science Foundation of China (22275185), the Major Research Project of Xiamen (3502Z20191015), and the Fujian Science & Technology Innovation Laboratory for Optoelectronic Information of China (2021ZR132, 2021ZZ115).

### Conflicts of interest

Chen YX is both the Junior Editorial Board Member of *Chemical Synthesis* and the guest editor of the Special Issue "Synthesis of Advanced Material for Novel Fuel Cells", while the other authors have declared that they have no conflicts of interest.

### Ethical approval and consent to participate

Not applicable.

### Consent for publication

Not applicable.

## Copyright

© The Author(s) 2024.

## REFERENCES

1. Bie C, Wang L, Yu J. Challenges for photocatalytic overall water splitting. *Chem* 2022;8:1567-74. DOI
2. Wang Z, Gu Y, Zheng L, et al. Machine learning guided dopant selection for metal oxide-based photoelectrochemical water splitting: the case study of Fe<sub>2</sub>O<sub>3</sub> and CuO. *Adv Mater* 2022;34:e2106776. DOI PubMed
3. Liu B, Wang S, Zhang G, et al. Tandem cells for unbiased photoelectrochemical water splitting. *Chem Soc Rev* 2023;52:4644-71. DOI PubMed
4. Li Y, Zhang D, Qiao W, et al. Nanostructured heterogeneous photocatalyst materials for green synthesis of valuable chemicals. *Chem Synth* 2022;2:9. DOI
5. Fujishima A, Honda K. Electrochemical photolysis of water at a semiconductor electrode. *Nature* 1972;238:37-8. DOI PubMed
6. Nayak AK, Sohn Y, Pradhan D. Facile green synthesis of WO<sub>3</sub>·H<sub>2</sub>O nanoplates and WO<sub>3</sub> nanowires with enhanced photoelectrochemical performance. *Cryst Growth Des* 2017;17:4949-57. DOI
7. Zhao HP, Zhu ML, Shi HY, et al. Cerium-doped iron oxide nanorod arrays for photoelectrochemical water splitting. *Molecules* 2022;27:9050. DOI PubMed PMC
8. Li C, Luo Z, Wang T, Gong J. Surface, bulk, and interface: rational design of hematite architecture toward efficient photoelectrochemical water splitting. *Adv Mater* 2018;30:e1707502. DOI PubMed
9. Tang P, Arbiol J. Engineering surface states of hematite based photoanodes for boosting photoelectrochemical water splitting. *Nanoscale Horiz* 2019;4:1256-76. DOI
10. Gao L, Chai H, Niu H, Jin J, Ma J. Roles of cobalt-coordinated polymeric perylene diimide in hematite photoanodes for improved water oxidation. *Small* 2023;19:e2302665. DOI PubMed
11. Wu J, Cheng Y, Lin J, Huang Y, Huang M, Hao S. Fabrication and photocatalytic properties of HLaNb<sub>2</sub>O<sub>7</sub>/(Pt, Fe<sub>2</sub>O<sub>3</sub>) pillared nanomaterial. *J Phys Chem C* 2007;111:3624-8. DOI
12. Wang H, Hu Y, Song G, Zheng D. Intrinsic and extrinsic doping to construct hematite nanorod p-n homojunctions for highly efficient PEC water splitting. *Chem Eng J* 2022;435:135016. DOI
13. Fujimoto H, Nakayasu B, Tobisu M. Synthesis of  $\gamma$ -lactams from acrylamides by single-carbon atom doping annulation. *J Am Chem Soc* 2023;145:19518-22. DOI PubMed
14. Li F, Yue X, Liao Y, Qiao L, Lv K, Xiang Q. Understanding the unique S-scheme charge migration in triazine/heptazine crystalline carbon nitride homojunction. *Nat Commun* 2023;14:3901. DOI PubMed PMC
15. Zhang M, Mao Y, Bao X, et al. Coupling benzylamine oxidation with CO<sub>2</sub> photoconversion to ethanol over a black phosphorus and bismuth tungstate S-scheme heterojunction. *Angew Chem Int Ed Engl* 2023;62:e202302919. DOI PubMed
16. Shen H, Qu F, Xia Y, Jiang X. Straightforward and ultrastable surface modification of microfluidic chips with norepinephrine bitartrate improves performance in immunoassays. *Anal Chem* 2018;90:3697-702. DOI PubMed
17. Li Z, Zhang Z. Tetrafunctional Cu<sub>2</sub>S thin layers on Cu<sub>2</sub>O nanowires for efficient photoelectrochemical water splitting. *Nano Res* 2018;11:1530-40. DOI
18. Guo K, Liu Z, Zhou C, et al. Fabrication of TiO<sub>2</sub> nano-branched arrays/Cu<sub>2</sub>S composite structure and its photoelectric performance. *Appl Catal B Environ* 2014;154-5:27-35. DOI
19. He B, Wang Y, Liu X, et al. Spatial engineering of a Co(OH)<sub>x</sub> encapsulated p-Cu<sub>2</sub>S/n-BiVO<sub>4</sub> photoanode: simultaneously promoting charge separation and surface reaction kinetics in solar water splitting. *J Mater Chem A* 2019;7:6747-52. DOI
20. Zhang Y, Huang Y, Zhu SS, et al. Covalent S-O bonding enables enhanced photoelectrochemical performance of Cu<sub>2</sub>S/Fe<sub>2</sub>O<sub>3</sub> heterojunction for water splitting. *Small* 2021;17:e2100320. DOI PubMed
21. Wu Y, Yao S, Lv G, et al. Construction of p-n junctions in single-unit-cell ZnIn<sub>2</sub>S<sub>4</sub> nanosheet arrays toward promoted photoelectrochemical performance. *J Catal* 2021;401:262-70. DOI
22. Li Z, Li J, Wang W, et al. Near zero-threshold voltage P-N junction diodes based on super-semiconducting nanostructured Ag/Al arrays. *Adv Mater* 2023;35:e2210612. DOI PubMed
23. Zhao Y, Westerik P, Santbergen R, Zoethout E, Gardeniers H, Bieberle-hütter A. From geometry to activity: a quantitative analysis of WO<sub>3</sub>/Si micropillar arrays for photoelectrochemical water splitting. *Adv Funct Mater* 2020;30:1909157. DOI
24. Meng L, Zhou X, Wang S, et al. A plasma-triggered O-S bond and P-N junction near the surface of a SnS<sub>2</sub> nanosheet array to enable efficient solar water oxidation. *Angew Chem Int Ed Engl* 2019;58:16668-75. DOI PubMed
25. Wu Y, Liu X, Zhang H, et al. Atomic sandwiched p-n homojunctions. *Angew Chem Int Ed Engl* 2021;60:3487-92. DOI PubMed
26. McDonald KJ, Choi KS. Photodeposition of Co-based oxygen evolution catalysts on  $\alpha$ -Fe<sub>2</sub>O<sub>3</sub> photoanodes. *Chem Mater* 2011;23:1686-93. DOI
27. Yang G, Li Y, Pang H, Chang K, Ye J. Ultrathin cobalt-manganese nanosheets: an efficient platform for enhanced photoelectrochemical water oxidation with electron-donating effect. *Adv Funct Mater* 2019;29:1904622. DOI
28. Yang Z, Jiang Y, Zhang W, et al. Solid-state, low-cost, and green synthesis and robust photochemical hydrogen evolution performance of ternary TiO<sub>2</sub>/MgTiO<sub>3</sub>/C photocatalysts. *iScience* 2019;14:15-26. DOI PubMed PMC
29. An Y, Lin C, Dong C, et al. Scalable photoelectrochemical cell for overall solar water splitting into H<sub>2</sub> and H<sub>2</sub>O<sub>2</sub>. *ACS Energy Lett*

- 2024;9:1415-22. DOI
30. Cao Q, Che R, Chen N. Scalable synthesis of Cu<sub>2</sub>S double-superlattice nanoparticle systems with enhanced UV/visible-light-driven photocatalytic activity. *Appl Catal B Environ* 2015;162:187-95. DOI
  31. Li J, Li J, Yuan H, Zhang W, Jiao Z, Song Zhao X. Modification of BiVO<sub>4</sub> with partially covered  $\alpha$ -Fe<sub>2</sub>O<sub>3</sub> spindles serving as hole-transport channels for significantly improved photoelectrochemical performance. *Chem Eng J* 2020;398:125662. DOI
  32. Yi S, Wulan B, Yan J, Jiang Q. Highly efficient photoelectrochemical water splitting: surface modification of cobalt-phosphate-loaded Co<sub>3</sub>O<sub>4</sub>/Fe<sub>2</sub>O<sub>3</sub> p-n heterojunction nanorod arrays. *Adv Funct Mater* 2019;29:1801902. DOI
  33. Gota S, Guiot E, Henriot M, Gautier-soyer M. Atomic-oxygen-assisted MBE growth of  $\alpha$ -Fe<sub>2</sub>O<sub>3</sub> on  $\alpha$ -Al<sub>2</sub>O<sub>3</sub> (0001): metastable FeO(111)-like phase at subnanometer thicknesses. *Phys Rev B* 1999;60:14387-95. DOI
  34. Liu P, Hensen EJ. Highly efficient and robust Au/MgCuCr<sub>2</sub>O<sub>4</sub> catalyst for gas-phase oxidation of ethanol to acetaldehyde. *J Am Chem Soc* 2013;135:14032-5. DOI PubMed
  35. Wang G, Ling Y, Wheeler DA, et al. Facile synthesis of highly photoactive  $\alpha$ -Fe<sub>2</sub>O<sub>3</sub>-based films for water oxidation. *Nano Lett* 2011;11:3503-9. DOI PubMed
  36. Abraham KM, Chaudhri SM. The lithium surface film in the Li/SO<sub>2</sub> cell. *J Electrochem Soc* 1986;133:1307-11. DOI
  37. Benoist L, Gonbeau D, Pfister-Guillouzo GP, Schmidt E, Meunier G, Levasseur A. XPS analysis of oxido-reduction mechanisms during lithium intercalation in amorphous molybdenum oxysulfide thin films. *Solid State Ionics* 1995;76:81-9. DOI
  38. Liang Y, Wang H, Zhou J, et al. Covalent hybrid of spinel manganese-cobalt oxide and graphene as advanced oxygen reduction electrocatalysts. *J Am Chem Soc* 2012;134:3517-23. DOI PubMed
  39. Xu Y, Wang X, Chen H, Kuang D, Su C. Toward high performance photoelectrochemical water oxidation: combined effects of ultrafine cobalt iron oxide nanoparticle. *Adv Funct Mater* 2016;26:4414-21. DOI
  40. Nie R, Shi J, Du W, Ning W, Hou Z, Xiao F. A sandwich N-doped graphene/Co<sub>3</sub>O<sub>4</sub> hybrid: an efficient catalyst for selective oxidation of olefins and alcohols. *J Mater Chem A* 2013;1:9037. DOI
  41. Kim H, Park J, Park I, et al. Coordination tuning of cobalt phosphates towards efficient water oxidation catalyst. *Nat Commun* 2015;6:8253. DOI PubMed PMC
  42. He B, Jia S, Zhao M, et al. General and robust photothermal-heating-enabled high-efficiency photoelectrochemical water splitting. *Adv Mater* 2021;33:e2004406. DOI PubMed
  43. Zhang Y, Liu Y, Gong X, et al. Construction of piezoelectric photocatalyst Au/BiVO<sub>4</sub> for efficient degradation of tetracycline and studied at single-particle level. *Chem Synth* 2024;4:21. DOI
  44. Tong M, Wang T, Lin S, et al. Ultra-thin carbon doped TiO<sub>2</sub> nanotube arrays for enhanced visible-light photoelectrochemical water splitting. *Appl Surf Sci* 2023;623:156980. DOI
  45. Tong MH, Chen YX, Wang TM, et al. Cerium synchronous doping in anatase for enhanced photocatalytic hydrogen production from ethanol-water mixtures. *Molecules* 2023;28:2433. DOI PubMed PMC
  46. Jiang X, Zhou J, Liu H, Chen Y, Lu C. Lotus pollen-templated synthesis of C, N, P-self doped KTi<sub>2</sub>(PO<sub>4</sub>)<sub>3</sub>/TiO<sub>2</sub> for sodium ion battery. *Colloid Surface A* 2022;650:129605. DOI
  47. Zhou Q, Chen Y, Shi H, et al. The construction of p/n-Cu<sub>2</sub>O heterojunction catalysts for efficient CO<sub>2</sub> photoelectric reduction. *Catalysts* 2023;13:857. DOI
  48. Tong M, Chen Y, Lin S, et al. Synchronous electrochemical anodization: a novel strategy for preparing cerium doped TiO<sub>2</sub> nanotube arrays toward visible-light PEC water splitting. *Electrochim Acta* 2023;463:142793. DOI
  49. Zhang Y, Xu L, Liu B, et al. Engineering BiVO<sub>4</sub> and oxygen evolution cocatalyst interfaces with rapid hole extraction for photoelectrochemical water splitting. *ACS Catal* 2023;13:5938-48. DOI
  50. Xiao J, Fan L, Huang Z, et al. Functional principle of the synergistic effect of co-loaded Co-Pi and FeOOH on Fe<sub>2</sub>O<sub>3</sub> photoanodes for photoelectrochemical water oxidation. *Chinese J Catal* 2020;41:1761-71. DOI
  51. Hu Z, Wang R, Han C, Chen R. Plasmon-induced hole-depletion layer on p-n heterojunction for highly efficient photoelectrochemical water splitting. *J Colloid Interface Sci* 2022;628:946-54. DOI PubMed